RSC Mechanochemistry

ROYAL SOCIETY OF CHEMISTRY

PAPER

View Article Online
View Journal

Cite this: DOI: 10.1039/d5mr00043b

Fluorination of mechanochemically synthesized metal–organic frameworks for PFAS adsorption in water†

Danilo Marchetti, [ab] Enrico Dalcanale, [a] Roberta Pinalli, [a] Mauro Gemmi, [b] Alessandro Pedrini *[a] and Chiara Massera *[a]

Received 4th April 2025
Accepted 26th May 2025

DOI: 10.1039/d5mr00043b

rsc.li/RSCMechanochem

Per- and poly-fluoroalkyl substances (PFAS) pose a significant environmental and health threat due to their persistence and widespread contamination of water sources. To address this challenge, this study explores the mechanochemical synthesis of two isoreticular highly interpenetrated MOFs, **TPPM-mCPW(Ph)** and **TPPM-mCPW(*p*-FPh)**, and investigates the influence of fluorine atoms decorating the framework on the affinity towards these pollutants. Furthermore, the dynamic structural responsiveness of these frameworks to external stimuli has been investigated. Adsorption experiments further highlighted the effect of framework fluorination on PFAS uptake, demonstrating its role in tuning material properties while maintaining structural connectivity. These results underline the potential of mechanochemistry in the discovery of novel metal–organic materials with promising applications in selective guest uptake.

Introduction

In recent years, the widespread presence of per- and poly-fluoroalkyl substances (PFAS) in the environment has raised concerns about this class of pollutants, since they have been linked to a range of adverse health effects.[1] PFAS are a group of synthetic molecules composed of perfluoroalkyl moieties (C_nF_{2n+1}), which have been used in a wide range of applications due to their high thermal and chemical stability.[2,3] However, PFAS chemical stability is also the cause of their long term persistence in the environment and bioaccumulation in living organisms. Various adsorption-based technologies have been developed to remove this class of pollutants from contaminated aqueous media.[4–7]

Recently, the use of metal–organic frameworks (MOFs) has shown promising results in the removal of PFAS from water.[8] MOFs are a class of hybrid organic–inorganic crystalline materials formed by the self-assembly of metal ions or clusters coordinated with organic linkers, resulting in highly porous structures.[9] First introduced in the 1990s, MOFs have earned significant interest due to their exceptional tunability, large surface area, and potential for applications in various fields, including gas storage, catalysis, drug delivery, and environmental remediation.[10] In addition, recent advances in MOFs research have expanded their utility to emerging areas such as energy storage[11] and water purification.[12] The design of these materials can be finely tuned to increase their affinity toward PFAS, which could be captured in the framework through electrostatic interactions, hydrophobic interactions, hydrogen bonds or halogen bonds.[8,13–20]

Among the various possible modifications, the incorporation of fluorine-substituted ligands (*e.g.*, F, CF_3) can significantly enhance not only the robustness and performance of MOFs under humid conditions but also their host–guest interactions.[21] Due to their high electronegativity, small atomic radius, and ability to form strongly polarized bonds, the introduction of fluorine atoms into MOF structures has been found to effectively increase the adsorption of carbon dioxide,[22] water,[23] and other small molecules such as light hydrocarbons.[24] Moreover, the presence of electronegative fluorine atoms alters the charge distribution on the pore surface, leading to the formation of an induced electric field gradient that can increase the interaction with less polarizable molecules such as fluorinated gases.[25] Fluorination has recently been indicated as an effective strategy to increase perfluoro octanoic acid (PFOA) uptake by UiO-67,[26,27] but its role in MOFs sequestration of PFAS requires further investigation.

MOFs are generally obtained by solvothermal reactions; however, more environmentally friendly methods to avoid the extensive use of organic solvents are desirable and have been actively researched. In this respect, mechanochemistry is a valid green alternative, significantly minimizing solvent usage and excess reagents in the synthetic process.[28,29] Moreover, it

[a]*Department of Chemistry, Life Sciences and Environmental Sustainability, INSTM UdR Parma, University of Parma, Parco Area delle Scienze 17/A, 43124, Parma, Italy. E-mail: chiara.massera@unipr.it; alessandro.pedrini@unipr.it*

[b]*Center for Materials Interfaces, Electron Crystallography, Istituto Italiano di Tecnologia, Viale Rinaldo Piaggio 34, 56025 Pontedera, Italy*

† Electronic supplementary information (ESI) available. CCDC 2440128–2440131. For ESI and crystallographic data in CIF or other electronic format see DOI: https://doi.org/10.1039/d5mr00043b

potentially allows to achieve high conversion while reducing energy consumption and chemical waste.[30]

In addition, mechanochemistry can be exploited to gain access to phases or structures that are difficult or impossible to obtain *via* conventional approaches.[31,32] All these advantages have funnelled research towards an efficient mechanochemical synthesis of MOFs over the past ten years.[33–39] Mechanochemical synthesis typically yields polycrystalline materials with small crystallite size and multiple twinning, making structural characterisation through conventional solid-state methods such as X-ray diffraction on single crystals or X-ray powder diffraction extremely challenging. However, this challenge can be faced by the use of 3D electron diffraction, which enables the analysis of single nanocrystals and is therefore a powerful tool to unlock the full potential of mechanochemistry for materials discovery.[40–43]

In this study, two new isoreticular flexible metal–organic frameworks, namely **TPPM-mCPW** MOFs, were obtained through mechanochemical synthesis (Fig. 1a). These MOFs are composed of tetra-4-(4-pyridil)phenylmethane (TPPM)[44] molecules coordinated in apical position to Cu(II) paddle-wheels (CPW) and discrete, mononuclear Cu(II) complexes (m), respectively (Fig. 1b), as secondary building units (SBUs). The combination of tetrahedral linkers (TPPM) with linear SBUs leads to highly interpenetrated diamond-like (***dia***) networks exhibiting reversible transition between open- and closed-pore forms. Similar to recently reported **TPPM-CPW** MOFs (see ESI†),[45] which feature an easily tuneable network held together solely by CPW units, the properties of the framework can be influenced by the residual groups surrounding the SBUs near the pore surfaces. The previously reported **TPPM-CPW(Ph)** MOF exhibits a remarkable stability in aqueous conditions (Fig. S2†), and affinity towards fluorinated anaesthetics in the gas phase. This inspired us to further investigate the role of fluorination of these materials towards the adsorption of fluorinated pollutants, namely PFAS, from water. For this purpose, the framework was functionalised through the introduction of specific fluorinated SBUs composed of *p*-fluorobenzene moieties. In contrast to **TPPM-CPW(Ph)**, the Cu(II) paddle wheels are functionalized in the equatorial position with *p*-fluorobenzoate ligands (*p*-$FPhCO_2^-$) in the complex $[Cu_2(p\text{-}FPhCO_2)_4(ACN)_2]$, leading to **CPW(*p*-FPh)** SBUs (Fig. 1b).

Results and discussion

Synthesis and structure elucidation of fluorinated TPPM-mCPW MOF

The synthesis of **TPPM-mCPW(*p*-FPh)** was carried out under analogous conditions to those employed for **TPPM-CPW(Ph)** (see

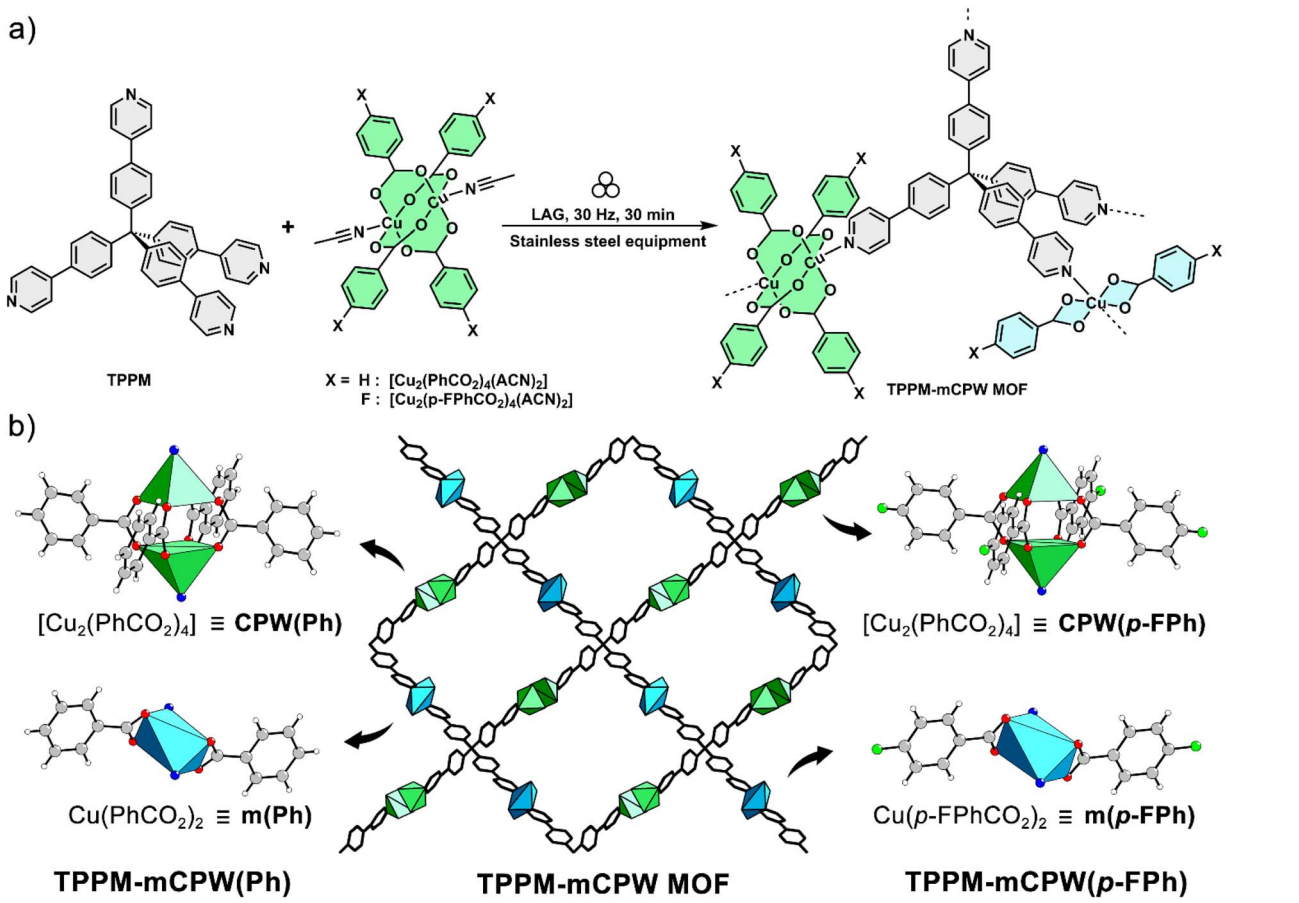

Fig. 1 (a) Reaction scheme employed for the mechanochemical synthesis of TPPM-mCPW MOFs. (b) Schematic representation of the TPPM-mCPW MOF architecture, in which the CPWs and the octahedral Cu(II) complexes have been represented as green and blue polyhedra, respectively.

ESI†).[45] The reaction was conducted in stainless steel jars filled with TPPM, *p*-fluorobenzoic acid (*p*-FPhA), $[Cu_2(p\text{-}FPhCO_2)_4(ACN)_2]$, and a mixture of benzyl alcohol (BnOH) and *N*,*N*-dimethylformamide (DMF) as liquid additive. The obtained powder was analysed by powder X-ray diffraction (PXRD), highlighting a diffraction profile that, in terms of peaks positions, does not correspond to any **TPPM-CPW(Ph)** phases (Fig. S3†) nor to any known structure. This indicates that even small modifications of the SBU precursor alter the reaction outcome. At this stage, the structural elucidation of the product was hampered by its low crystallinity, with a drop of the diffraction signal in the PXRD pattern beyond 30° in 2θ. Thus, a different synthetic approach was employed to obtain a well-diffracting material. Three different solutions containing TPPM, *p*-FPhA and $[Cu_2(p\text{-}FPhCO_2)_4(ACN)_2]$ in a mixture of $^{i}PrOH/CHCl_3$ were brought into contact by layering and heated up at 80 °C for 3 days (see ESI†). The reaction was conducted with a large excess of *p*-FPhA as modulating agent, to obtain crystalline domains larger than those obtained through mechanochemical synthesis. The resulting product showed the same PXRD profile as the mechanochemical one, but with sharper diffraction peaks (Fig. S4†). The presence of nanometric crystalline domains not suitable for single-crystal X-ray diffraction (SC-XRD) analysis prompted us to rely on 3D electron diffraction (3D ED) to solve the structure. This emerging technique uses a single-crystal diffraction protocol to efficiently determine the structure of compounds with crystal sizes too small for SC-XRD analysis.[46–50] The product was inserted into a specifically equipped transmission electron microscope (TEM) and an initial scanning transmission electron microscopy (STEM) image revealed the presence of rod-shaped crystals (Fig. S15†). Moreover, due to the beam sensitivity of the material, the analysis had to be conducted using a special low-dose setup, in which the electron dose was kept below 0.05 el s^{-1} $Å^2$. The diffraction patterns were collected following a continuous rotation (cRED) protocol, where the parallel electron beam is scanning on a square area of 300 × 300 nm^2.[51] The reciprocal space reconstructed from the collected diffraction patterns indicates a primitive monoclinic lattice with parameters $a = 25.632(11)$ Å, $b = 7.653(2)$ Å, $c = 23.063(9)$ Å, $\beta = 98.12(3)°$. The unit cell determination from 3D ED data was validated using PXRD data through Le Bail refinement (Fig. S5†), showing a strong agreement between the two analyses (Table S2†). The indexed reflections were then integrated, and the crystal structure was solved *ab initio* on cRED data, in the space group *P*2/*n*, and refined with a kinematical approach.[46] The obtained structure revealed the presence of a fluorinated metal–organic framework, **TPPM-mCPW(p-FPh)**, possessing a different connectivity with respect to the previously reported **TPPM-CPW(Ph)** MOF.[44]

TPPM-mCPW(*p*-FPh) comprises $\{TPPM[Cu_2(p\text{-}FPhCO_2)_4][Cu(p\text{-}FPhCO_2)_2]\}_n$ repeating units, in which the TPPM molecules are respectively coordinated to a CPW and a Cu(II) octahedral complex (Fig. 1b). In both metal nodes, the TPPM molecules are coordinated in the apical positions of the complexes, while the benzoate ligands are disposed along the equatorial ones (Fig. 2a). **TPPM-mCPW(*p*-FPh)** forms a diamond-like network (***dia***-net) with a point symbol of $\{6^6\}$. In analogy to **TPPM-CPW(Ph)**, it also exhibits an eightfold interpenetration (Fig. 3a) with interwoven

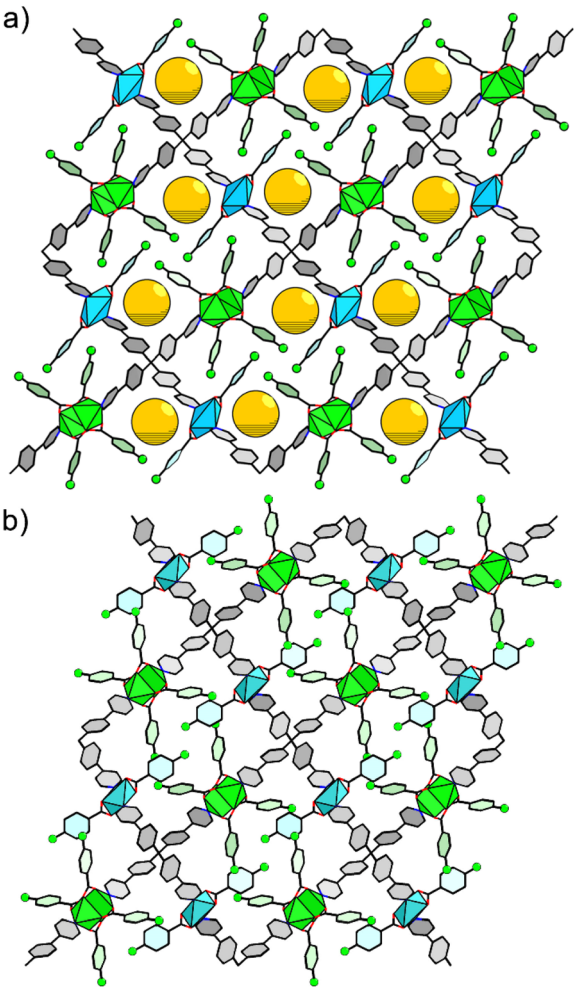

Fig. 2 Crystal structure expansion of (a) ***op*-TPPM-mCPW(*p*-FPh)** and (b) ***cp*-TPPM-mCPW(*p*-FPh)**, both oriented along their crystallographic *b*-axis; *op* = open pore; *cp* = closed pore. Copper atoms are shown as green and blue polyhedra; fluorine atoms as green spheres; oxygen, nitrogen, and carbon atoms as red, blue and black sticks, respectively. In ***op*-TPPM-mCPW(*p*-FPh)**, the *p*-FPhA molecules hosted in the cavity have been removed and replaced by yellow spheres, to highlight the location of the channels in the framework.

nets extended along the crystallographic *b*-axis and distanced by the axis length (Fig. S24†). This alignment gives rise to channels extended in that direction, contributing to a theoretical void of approximately 18.8% of the unit cell volume (840.74 $Å^3$, as calculated using Mercury4 software).[52] This open pore (*op*) phase, herein indicated as ***op*-TPPM-mCPW(*p*-FPh)**, presents channels divided into two mirrored cavities.

These cavities are respectively delimited on one side by TPPM molecules and on the other side by the substituents of the carboxylic groups coordinated to the metal centres, in this case *p*-fluorobenzoic groups. These aromatic moieties interact with each other through C–H···F interactions (Fig. S22†). Furthermore, from the obtained structural model, partially occupied *p*-FPhA molecules (site occupancy 0.75) were modelled inside the channels, which are involved in H-bond interactions with the polymeric backbone (Fig. S21d and S23†). This leads to

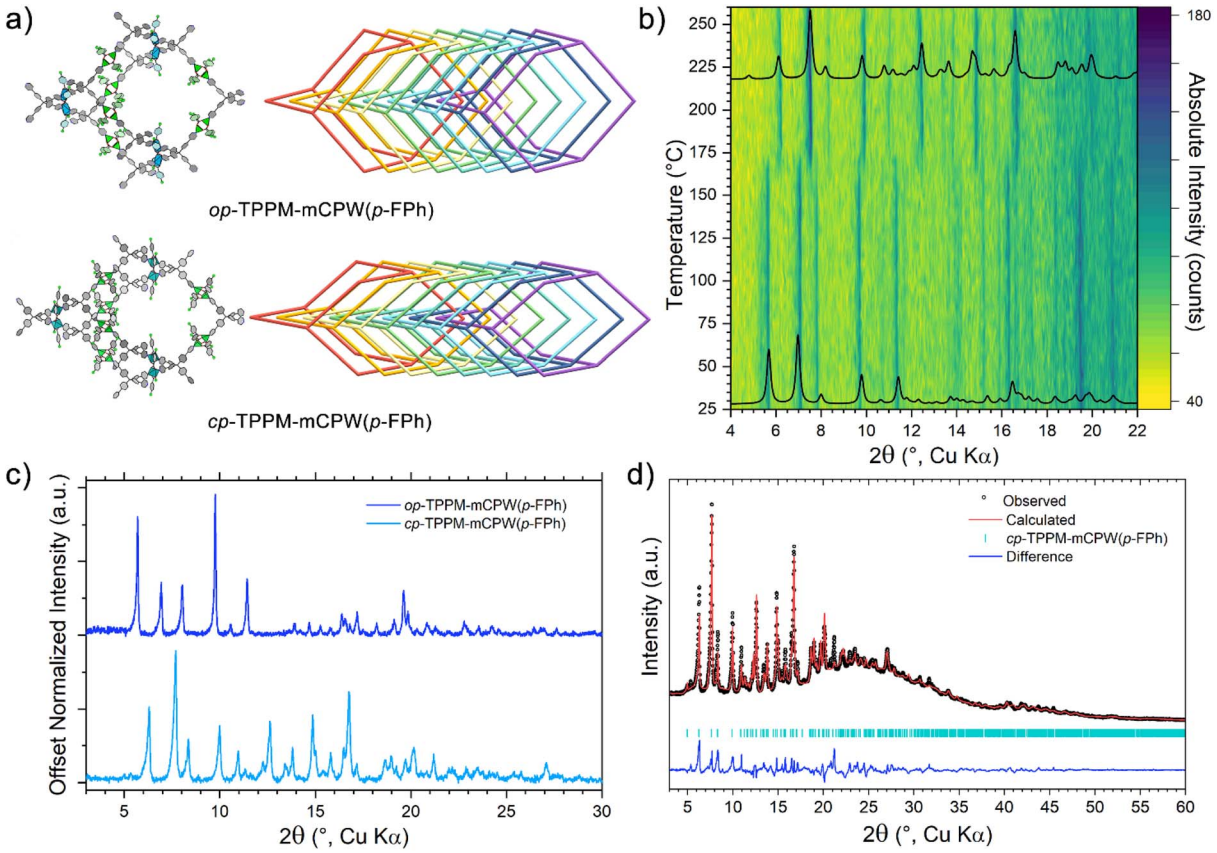

Fig. 3 (a) Schematization of the ***dia***-net and its eight-fold interpenetration for ***op*-TPPM-mCPW(*p*-FPh)** and ***cp*-TPPM-mCPW(*p*-FPh)**. (b) Temperature-induced phase transition of **TPPM-mCPW(*p*-FPh)**, between its *op* and *cp* forms, analysed by temperature-resolved *in situ* powder X-ray diffraction; 2D projection along the intensity axis. (c) PXRD profile comparison between ***op*-TPPM-mCPW(*p*-FPh)** before and after the purification process. The pattern of the purified phase was labelled ***cp*-TPPM-mCPW(*p*-FPh)**, as the purification induces a phase transition to this closed pore form (Fig. S6 and S7†). (d) Profile fit from Rietveld refinement on ***cp*-TPPM-mCPW(*p*-FPh)**. The range is shown for 2θ values of 3–60° for clarity, whereas the refinement was carried out in the range 3–80°. The refinement converged to $R_p = 3.39\%$, $wR_p = 6.05\%$ and GOF = 2.29.

a structure with general formula $\{TPPM[Cu_2(p\text{-}FPhCO_2)_4][Cu(p\text{-}FPhCO_2)_2\}_n \cdot n0.75(p\text{-}FPhCO_2H)$.

Dynamic behaviour of TPPM-mCPW(*p*-FPh)

The removal of the guest molecules through a solvent mixture capable of completely solubilizing the unreacted reagent alters the PXRD profile pattern of the previously described ***op*-TPPM-mCPW(*p*-FPh)** phase (Fig. S6†). The absence of included *p*-FPhA or solvent molecules in the washed and evacuated phase of **TPPM-mCPW(*p*-FPh)** was confirmed by TGA analysis, since the thermogram only displays a weight loss at 332 °C related to the thermal degradation of the material (Fig. S26†). These results suggest the presence of a dynamic system that, in analogy with **TPPM-CPW** MOFs, can change its crystal structure upon external stimuli. Notably, after the same treatment, both mechanochemically and solvothermally synthesized **TPPM-mCPW(*p*-FPh)** MOFs exhibit analogous PXRD profiles, indicating that this behaviour is not influenced by the dimension of the crystalline domains (Fig. S7†).

Since **TPPM-mCPW(*p*-FPh)** changes its crystalline phase upon removal of guest molecules, a temperature-resolved *in situ* PXRD analysis was carried out on the crude product to further investigate this behaviour. This experiment revealed that, upon heating, ***op*-TPPM-mCPW(*p*-FPh)** undergoes a phase transition around 170 °C and a crystalline phase with a powder profile congruent to the pattern of the washed product appears (Fig. 3b and c). This result confirms that, after the removal of the guest molecules embedded in the channels, the **TPPM-mCPW(*p*-FPh)** framework maintains its crystallinity, leading to a new structural arrangement. To elucidate the structure of the activated **TPPM-mCPW(*p*-FPh)** phase, an indexing process followed by a Pawley refinement was conducted over its PXRD data, revealing a monoclinic system with lattice parameters a = 21.84(5) Å, b = 8.117(18) Å, c = 23.74(5) Å, β = 103.302(5)°. This denotes a shrinking effect on the crystallographic a-axis followed by an increase in the β-angle.

Furthermore, the crystal structure of the phase was obtained by simulated annealing and then refined through a Rietveld approach (Fig. 3d). The retrieved model shows a contracted **TPPM-mCPW(*p*-FPh)** framework displaying isolated voids instead of channels along the crystallographic b-axis (Fig. S21b†). These results prompted us to consider this phase as a closed pore (*cp*) form, ***cp*-TPPM-mCPW(*p*-FPh)** (Fig. 2b, 3a and S25†).

Preparation of a non-fluorinated TPPM-mCPW MOF

With the aim of investigating the effect of fluorination towards the adsorption of PFAS, a non-fluorinated counterpart of **TPPM-mCPW(*p*-FPh)** was prepared. The synthesis of ***op*-TPPM-mCPW(Ph)** was carried out *via* liquid-assisted grinding (LAG) employing TPPM and $[Cu_2(PhCO_2)_4(ACN)_2]$ as solid reagents. The reaction was conducted in a stainless-steel jar at 30 Hz for 30 minutes leading to a product with a PXRD pattern equivalent to that of ***op*-TPPM-mCPW(*p*-FPh)** (Fig. S9†). Also in this case, to facilitate the determination of the crystal structure of ***op*-TPPM-mCPW(Ph)**, a solvothermal synthesis was carried out, which permitted to extend its crystalline domains (Fig. S12†). The micrometric crystals thus obtained (Fig. S16†) were characterised by 3D ED analysis. From the reciprocal space reconstruction, the sample was indexed in the monoclinic primitive lattice with parameters $a = 25.534(7)$ Å, $b = 7.485(3)$ Å, $c = 22.287(9)$ Å, $\beta = 98.81(3)°$ (Table S6†). The unit cell determination from 3D ED data was validated on PXRD data through Le Bail refinement (Fig. S13†), showing a strong agreement between the two analyses (Table S3†). The indexed data were integrated up to 0.80 Å of resolution and the structural model was solved *ab initio*, in the space group $P2/n$, through the Superflip software.[53] The obtained model was refined kinematically, revealing the formation of an ***op*-TPPM-mCPW(Ph)** MOF, showing the same interpenetrated net of its fluorinated counterpart and channels oriented along the crystallographic *b*-axis (Fig. 4a and b), with a theoretical void accounting for 16.7% of the unit cell volume (703.92 Å^3, Fig. S21c†). Moreover, from the kinematical refinement, it was possible to identify the solvent molecules (DMF) embedded in those channels (Fig. S20 and S21e†).

Thus, the ***op*-TPPM-mCPW(Ph)** asymmetric unit was modelled with a single DMF molecule presenting an occupancy of 0.5. The partial occupancy of these solvent molecules is also supported by TGA analysis, which shows a weight loss attributable to a DMF stoichiometry of 0.35 (Fig. S27†). The resulting framework, despite the different SBU functionalization, exhibits a channel diameter comparable to that of ***op*-TPPM-mCPW(*p*-FPh)** and suitable for hosting the PFAS molecules used in the subsequent uptake studies (Tables S9 and S10†).

Also for **TPPM-mCPW(Ph)**, solvent exchange and evacuation steps modified the PXRD profile leading to the appearance of a new crystalline phase (Fig. S10†). However, differently to **TPPM-mCPW(*p*-FPh)**, the non-fluorinated MOF shows only a partial conversion to a contracted phase, as indicated by the

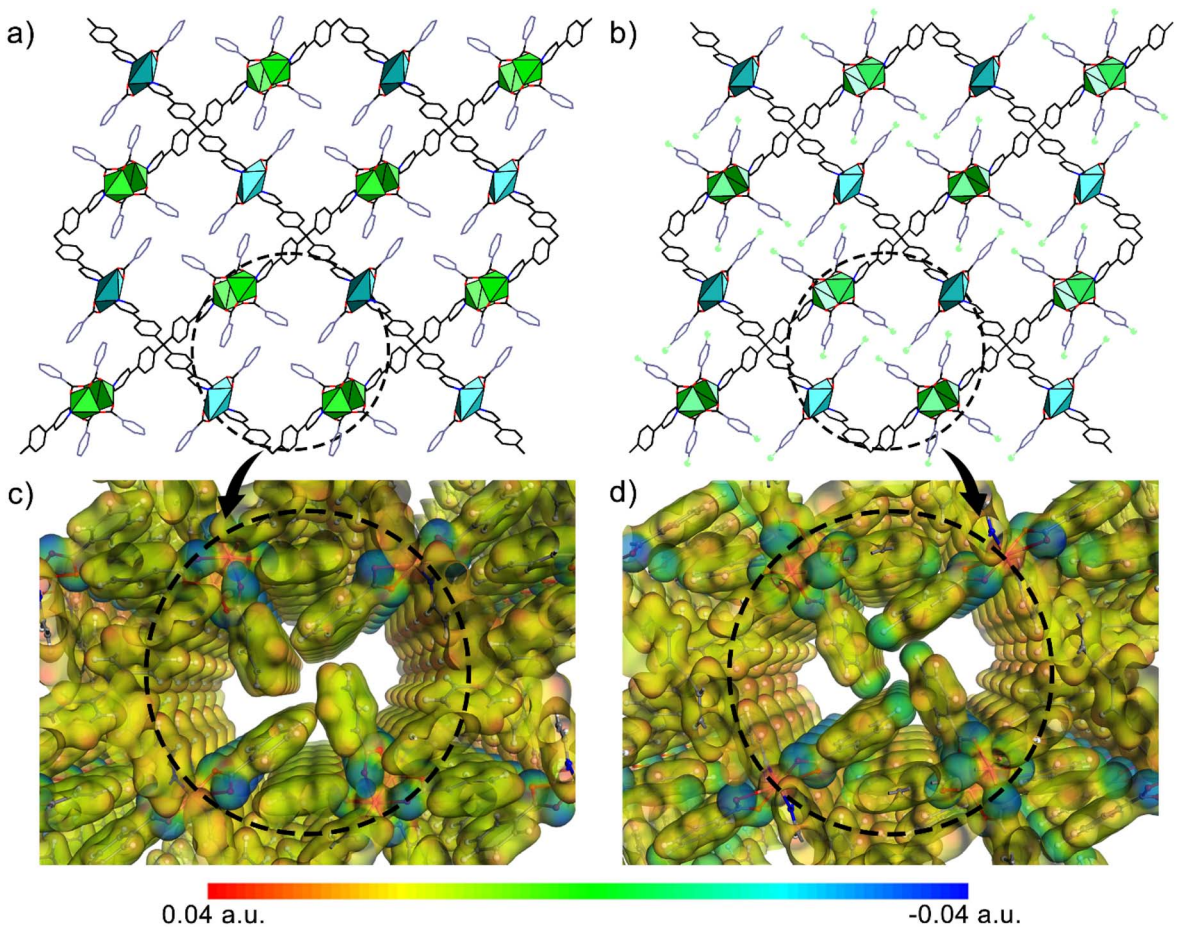

Fig. 4 Comparison between the crystal expansion of (a) *op*-TPPM-mCPW(Ph) and (b) *op*-TPPM-mCPW(*p*-FPh), followed by their potential electrostatic surfaces (c and d). For both MOFs, the structure has been oriented along the crystallographic *b*-axis. The surfaces have been calculated at the M06-L level of theory using the DMol^3 package of the Materials Studio software.[54]

presence of spurious peaks in the diffraction pattern. A complete conversion of ***op*-TPPM-mCPW(Ph)** to ***cp*-TPPM-mCPW(Ph)** was achieved only by a heating process around 180 °C, as confirmed by thermal and *in situ* PXRD analyses (Fig. S14†).

PFAS adsorption studies

For their simple, fast and efficient preparation conditions, combined with lower energy requirements for the activation processes, and comparable particle size distribution (Fig. S37†), only mechanochemically synthesized **TPPM-mCPW** MOFs were selected as candidates for the investigation of PFAS adsorption. As an essential property for materials used in PFAS removal processes, their stability in aqueous media was verified.[20,26,55] The stability tests were conducted on both ***cp*-TPPM-mCPW(*p*-FPh)** and ***cp*-TPPM-mCPW(Ph)** by suspending them in water for one week. The PXRD patterns were then collected and confirmed the retention of crystallinity and the applicability of these materials for water remediation (Fig. S8†).

After assessing the stability of the MOFs in aqueous media, adsorption tests were carried out to investigate the role of fluorination on the affinity of **TPPM-mCPW** MOFs towards PFAS. In particular, the sodium salts of perfluorobutanoic acid (NaPFB) and perfluorooctanoic acid (NaPFO) were selected as target molecules. These two pollutants are among the most studied PFAS and, due to their different chain lengths, exhibit contrasting properties in terms of solubility and hydrophobicity.[18,56] The PFAS adsorption capacity was evaluated for the closed pore forms of **TPPM-mCPW(*p*-FPh)** and **TPPM-mCPW(Ph)** to avoid guest molecule interference. The ***cp*-TPPM-mCPW** MOFs were exposed to a 5 mM aqueous solution of each target molecule for 24 h. The solid was recovered, washed with distilled water, and the presence of PFAS estimated through ^{19}F NMR analysis after digestion with a DCl/D_2O (2 : 8) solution and complete solubilization in DMSO-d_6 (Fig. 5a).

For its low hydrophobicity, neither ***cp*-TPPM-mCPW(Ph)** nor ***cp*-TPPM-mCPW(*p*-FPh)** were found to absorb NaPFB (Fig. S28 and S30†). In contrast, the experiments conducted on NaPFO demonstrated the capability of ***cp*-TPPM-mCPW(*p*-FPh)** to adsorb a moderate amount (around 25% in moles) of NaPFO (Fig. 5b and S31–S34†). On the other hand, in the ^{19}F NMR of digested ***cp*-TPPM-mCPW(Ph)**, no signals associated with the presence of NaPFO were detected, indicating a negligible affinity for this class of contaminants (Fig. S29†). Moreover, the calculation of the electrostatic potential map shows, for both frameworks, a negative charge surrounding the carboxylic oxygen facing the inner side of the cavities (Fig. 4c and d). In addition, **TPPM-mCPW(*p*-FPh)** displays a negative potential in the proximity of the fluorine atoms, which highlights the potential regions for F···F contacts along the cavities. The propensity of NaPFO to interact with **TPPM-mCPW(*p*-FPh)** can be related to F···F interactions and a more pronounced hydrophobic effect, both resulting from the framework fluorination.[8,13–17]

Subsequently, the ***cp*-TPPM-mCPW(*p*-FPh)** that had been exposed to NaPFO was characterized by PXRD analysis to check

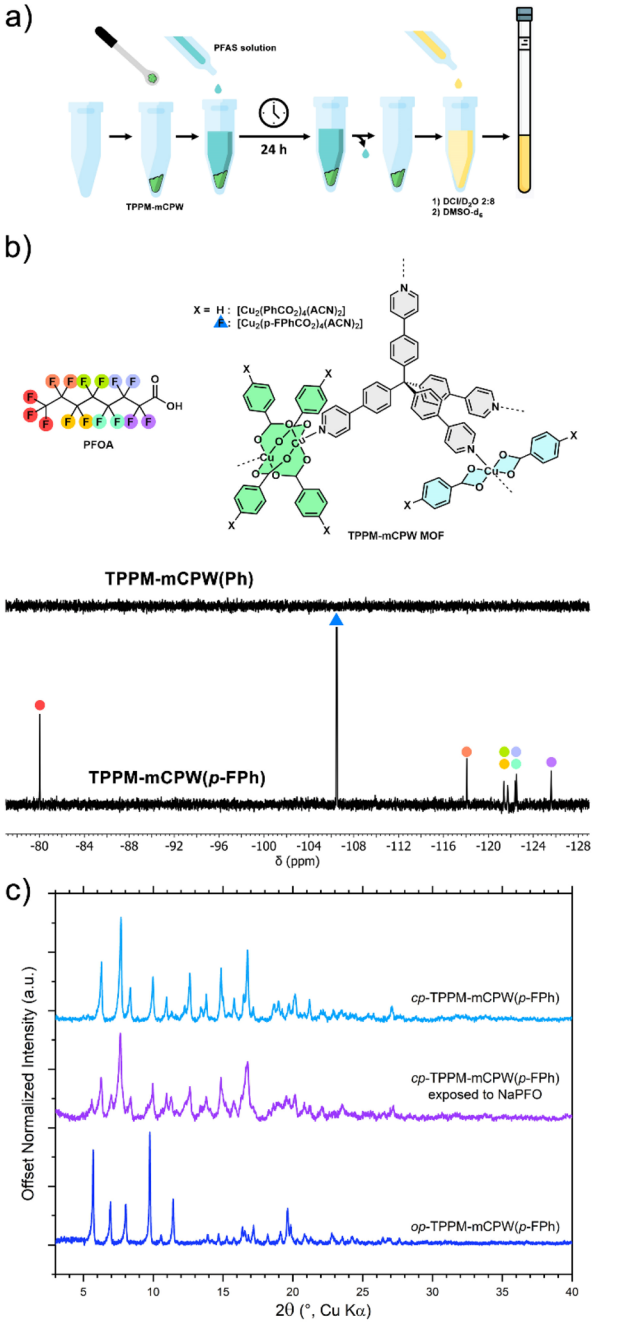

Fig. 5 (a) Schematic representation of the PFAS exposure experiment conducted on the ***cp*-TPPM-mCPW MOFs**. (b) ^{19}F NMR spectrum of digested **TPPM-mCPW(Ph)** and **TPPM-mCPW(*p*-FPh)** after exposure to the NaPFO solution. Details of the experiment have been reported in the dedicated section of the ESI.† (c) PXRD profile comparison between the ***cp*-TPPM-mCPW(*p*-FPh)** exposed to NaPFO with its corresponding *op* and *cp* pure phases.

for any structural changes after the adsorption experiment. The obtained PXRD profile differs from the initial one, displaying the co-presence of both *cp* and *op* forms of **TPPM-mCPW(*p*-FPh)**. As the PFAS exposure experiment started from the close pore form of **TPPM-mCPW(*p*-FPh)**, the observation of the ***op*-TPPM-mCPW(*p*-F*Ph*)** diffraction pattern demonstrates that this material can expand its framework when exposed to specific

guest molecules (Fig. 5c). The observed partial conversion to ***op*-TPPM-mCPW(*p*-FPh)** can be explained considering that the adsorption process takes place primarily at the surface of the material.

To further assess the NaPFO uptake of ***cp*-TPPM-mCPW(*p*-FPh)** from aqueous solution, an adsorption isotherm was collected by exposing this MOF to different concentrations of NaPFO, using trifluoroethanol (TFE) as internal standard. The uptake was estimated through ^{19}F NMR analysis, in which, for all the spectra, the area of the signal associated with the CF_3 of NaPFO was compared with the one of the same group of TFE (Fig. S35†). The obtained uptake values were plotted against concentration, and a Langmuir fit was applied to estimate a maximum adsorption capacity of 336 mg g^{-1} and adsorption equilibrium constant of 3.9×10^{-3} L mg^{-1} (Fig. S36 and Table S8†). These results are consistent with the values calculated from the structural data of the ***op*-TPPM-mCPW(*p*-FPh)** phase, which indicate a maximum theoretical adsorption of 353 mg g^{-1} (see ESI†).

Conclusions

In this work, two isoreticular, highly interpenetrated MOFs, **TPPM-mCPW(*p*-FPh)** and **TPPM-mCPW(Ph)**, have been prepared by mechanochemical synthesis. The LAG reactions were carried out by combining a tetrahedral linker with linear Cu(II)-based SBUs, resulting in a ***dia*-network** with channels surrounded by the residual groups of the SBUs. Both networks exhibit phase transitions between open and closed pore forms when exposed to external stimuli such as temperature, solvent mixture or guest molecules. Their adsorption performance against two different PFAS solutions was evaluated using ^{19}F NMR, to investigate the influence of the framework fluorination on the uptake of this class of pollutants. Indeed, the presence of fluorine atoms in **TPPM-mCPW(*p*-FPh)** enhances its affinity towards NaPFO, showing its tendency to convert to the open pore form after exposure. Furthermore, the uptake was assessed by measuring the relative adsorption isotherm in aqueous media. In conclusion, this work highlights the potential of mechanochemical synthesis in the discovery of novel framework architectures and how the introduction of fluorination can influence their properties while preserving the framework connectivity.

Data availability

The data supporting this article have been included as part of the ESI.† The crystallographic data have been deposited with the Cambridge Crystallographic Data Centre as supplementary publication no. 2440128–2440131 and can be obtained free of charge on application to the CCDC, 12 Union Road, Cambridge, CB2 1EZ, UK (e-mail: deposit@ccdc.cam.ac.uk or **http://www.ccdc.cam.ac.uk**).

Author contributions

The manuscript was written through the contributions of all authors. All authors have given approval to the final version of the manuscript.

Conflicts of interest

There are no conflicts to declare.

Acknowledgements

This work has benefited from the equipment and framework of the COMP-HUB and COMP-R Initiatives, funded by the 'Departments of Excellence' program of the Italian Ministry for University and Research (MIUR, 2018–2022 and MUR, 2023–2027). Centro Interdipartimentale Misure "G. Casnati" is thanked for the use of NMR facilities. Chiesi Farmaceutici SpA is acknowledged for the support with the D8 Venture X-ray equipment. AP, CM and DM acknowledge financial support under the National Recovery and Resilience Plan (NRRP), Mission 4, Component 2, Investment 1.1, Call for tender No. 1409 published by MUR on 14.9.2022, Project title: ENLIGHTENING (ENgineering LIGHT-activated materials for the abatement of ENvironmentally hazardous and pollutING substances) – Project Code P2022PZ2MM – CUP Code D53D23016860001 – Funded by the European Union – NextGenerationEU. We acknowledge Prof. A. Ken Inge from Stockholm University for Materials Studio calculations.

Notes and references

1 S. E. Fenton, A. Ducatman, A. Boobis, J. C. DeWitt, C. Lau, C. Ng, J. S. Smith and S. M. Roberts, *Environ. Toxicol. Chem.*, 2020, **40**, 606–630.
2 D. O'Hagan, *Chem. Soc. Rev.*, 2008, **37**, 308–319.
3 J. N. Meegoda, J. A. Kewalramani, B. Li and R. W. Marsh, *Int. J. Environ. Res. Public Health*, 2020, **17**, 8117.
4 X. Zhu, C. Cheng, X. Qin and Y. Wang, *J. Hazard. Mater.*, 2025, **485**, 136870.
5 Y. Zhu, R. Wang, Y. Zhou, W. Ma, J. Fan, X. Deng, C. Zhu, A. Yu, G. Xu, D.-S. Li and C. Sun, *Mater. Today Energy*, 2025, **49**, 101817.
6 F. Yang and Z. Li, *Emerging Contam.*, 2025, **11**, 100464.
7 A. Pramanik, O. P. Kolawole, S. Kundu, K. Gates, S. Rai, M. K. Shukla and P. C. Ray, *ACS Omega*, 2024, **9**, 49452–49462.
8 L. I. FitzGerald, J. F. Olorunyomi, R. Singh and C. M. Doherty, *ChemSusChem*, 2022, **15**, e202201136.
9 H.-C. Zhou, J. R. Long and O. M. Yaghi, *Chem. Rev.*, 2012, **112**, 673–674.
10 H. Furukawa, K. E. Cordova, M. O'Keeffe and O. M. Yaghi, *Science*, 2013, **341**, 1230444.
11 Z. A. Sandhu, M. A. Raza, N. S. Awwad, H. A. Ibrahium, U. Farwa, S. Ashraf, A. Dildar, E. Fatima, S. Ashraf and F. Ali, *Mater. Adv.*, 2024, **5**, 30–50.
12 W. Li, P. Xu, Z. Wang, Y. He, H. Qin, Y. Zeng, Y. Li, Z. Zhang and J. Gao, *Mater. Chem. Front.*, 2023, **7**, 5140–5170.
13 S. Li, J. Ma, J. Cheng, G. Wu, S. Wang, C. Huang, J. Li and L. Chen, *Langmuir*, 2024, **40**, 2815–2829.
14 E. Loukopoulos, S. Marugán-Benito, D. Raptis, E. Tylianakis, G. E. Froudakis, A. Mavrandonakis and A. E. Platero-Prats, *Adv. Funct. Mater.*, 2024, **34**, 2409932.

15 B. Chen, Z. Yang, X. Qu, S. Zheng, D. Yin and H. Fu, *ACS Appl. Mater. Interfaces*, 2021, **13**, 47706–47716.
16 F. Ahmadi Tabar, J. W. Lowdon, S. Bakhshi Sichani, M. Khorshid, T. J. Cleij, H. Diliën, K. Eersels, P. Wagner and B. Van Grinsven, *Sensors*, 2023, **24**, 130.
17 T. S. Erkal, N. Shamsuddin, S. Kirmizialtin and A. O. Yazaydin, *J. Phys. Chem. C*, 2023, **127**, 3204–3216.
18 C. Gomri, B. T. Benkhaled, M. Cretin and M. Semsarilar, *Macromol. Chem. Phys.*, 2024, **225**, 2400012.
19 L. Lu and C. Na, *ACS Omega*, 2024, **9**, 26050–26057.
20 R.-R. Liang, S. Xu, Z. Han, Y. Yang, K.-Y. Wang, Z. Huang, J. Rushlow, P. Cai, P. Samorì and H.-C. Zhou, *J. Am. Chem. Soc.*, 2024, **146**, 9811–9818.
21 D. Morelli Venturi and F. Costantino, *RSC Adv.*, 2023, **13**, 29215–29230.
22 J. Perego, C. X. Bezuidenhout, A. Pedrini, S. Bracco, M. Negroni, A. Comotti and P. Sozzani, *J. Mater. Chem. A*, 2020, **8**, 11406–11413.
23 R. Abazari, S. Sanati, N. Li and J. Qian, *Inorg. Chem.*, 2023, **62**, 18680–18688.
24 J. Ma, M. Zhang, R. Feng, L. Dong, W. Sun and Y. Jia, *Inorg. Chem. Front.*, 2024, **11**, 5636–5647.
25 W. Zhang, Y. Li, S. Wang, Y. Wu, S. Chen, Y. Fu, W. Ma, Z. Zhang and H. Ma, *ACS Appl. Mater. Interfaces*, 2022, **14**, 35126–35137.
26 D. Hedbom, P. Gaiser, T. Günther, O. Cheung, M. Strømme, M. Åhlén and M. Sjödin, *J. Mater. Chem. A*, 2025, **13**, 1731–1737.
27 K. Sini, D. Bourgeois, M. Idouhar, M. Carboni and D. Meyer, *New J. Chem.*, 2028, **42**, 17889–17894.
28 J. Alić, M. Schlegel, F. Emmerling and T. Stolar, *Angew. Chem., Int. Ed.*, 2024, **63**, e202414745.
29 K. J. Ardila-Fierro and J. G. Hernández, *ChemSusChem*, 2021, **14**, 2145–2162.
30 T. Friščić, C. Mottillo and H. M. Titi, *Angew. Chem., Int. Ed.*, 2020, **59**, 1018–1029.
31 J. L. Howard, Q. Cao and D. L. Browne, *Chem. Sci.*, 2018, **9**, 3080–3094.
32 W. Jones and M. D. Eddleston, *Faraday Discuss.*, 2014, **170**, 9–34.
33 T. Friščić, in *Encyclopedia of Inorganic and Bioinorganic Chemistry*, ed. R. A. Scott, Wiley, 2nd edn, 2014, pp. 1–19.
34 D. Chen, J. Zhao, P. Zhang and S. Dai, *Polyhedron*, 2019, **162**, 59–64.
35 T. Stolar and K. Užarević, *CrystEngComm*, 2020, **22**, 4511–4525.
36 H. M. Titi, J.-L. Do, A. J. Howarth, K. Nagapudi and T. Friščić, *Chem. Sci.*, 2020, **11**, 7578–7584.
37 J. Beamish-Cook, K. Shankland, C. A. Murray and P. Vaqueiro, *Cryst. Growth Des.*, 2021, **21**, 3047–3055.
38 E. Colacino, V. Isoni, D. Crawford and F. García, *Trends Chem.*, 2021, **3**, 335–339.
39 A. V. Desai, E. Lizundia, A. Laybourn, D. N. Rainer, A. R. Armstrong, R. E. Morris, S. Wuttke and R. Ettlinger, *Adv. Funct. Mater.*, 2024, **34**, 2304660.
40 D. Marchetti, F. Guagnini, A. E. Lanza, A. Pedrini, L. Righi, E. Dalcanale, M. Gemmi and C. Massera, *Cryst. Growth Des.*, 2021, **21**, 6660–6664.
41 T. Sasaki, T. Nakane, A. Kawamoto, T. Nishizawa and G. Kurisu, *CrystEngComm*, 2023, **25**, 352–356.
42 D. Marchetti, A. Pedrini, C. Massera, M. D. Faye Diouf, C. Jandl, G. Steinfeld and M. Gemmi, *Acta Crystallogr., Sect. B*, 2023, **79**, 432–436.
43 A. Sala, M. D. Faye Diouf, D. Marchetti, L. Pasquale and M. Gemmi, *Cryst. Growth Des.*, 2024, **24**, 3246–3255.
44 D. Marchetti, F. Portone, F. Mezzadri, E. Dalcanale, M. Gemmi, A. Pedrini and C. Massera, *Chem.–Eur. J.*, 2022, **28**, e202202977.
45 D. Marchetti, N. Riboni, A. K. Inge, O. Cheung, M. Gemmi, E. Dalcanale, F. Bianchi, C. Massera and A. Pedrini, *Chem. Mater.*, 2025, **37**, 2230–2240.
46 M. Gemmi, E. Mugnaioli, T. E. Gorelik, U. Kolb, L. Palatinus, P. Boullay, S. Hovmöller and J. P. Abrahams, *ACS Cent. Sci.*, 2019, **5**, 1315–1329.
47 M. Gemmi and A. E. Lanza, *Acta Crystallogr., Sect. B*, 2019, **75**, 495–504.
48 U. Kolb, T. Gorelik, C. Kübel, M. T. Otten and D. Hubert, *Ultramicroscopy*, 2007, **107**, 507–513.
49 U. Kolb, T. Gorelik and M. T. Otten, *Ultramicroscopy*, 2008, **108**, 763–772.
50 U. Kolb, E. Mugnaioli and T. E. Gorelik, *Cryst. Res. Technol.*, 2011, **46**, 542–554.
51 F. Bertocchi, D. Marchetti, S. Doria, M. Di Donato, C. Sissa, M. Gemmi, E. Dalcanale, R. Pinalli and A. Lapini, *Chem.–Eur. J.*, 2023, **30**, e202302619.
52 C. F. Macrae, I. Sovago, S. J. Cottrell, P. T. A. Galek, P. McCabe, E. Pidcock, M. Platings, G. P. Shields, J. S. Stevens, M. Towler and P. A. Wood, *J. Appl. Crystallogr.*, 2020, **53**, 226–235.
53 L. Palatinus and G. Chapuis, *J. Appl. Crystallogr.*, 2007, **40**, 786–790.
54 M. Meunier and S. Robertson, *Mol. Simul.*, 2021, **47**, 537–539.
55 Y. Jia, J. Qian and B. Pan, *Anal. Chem.*, 2021, **93**, 11116–11122.
56 S. Wacławek, K. Krawczyk, D. Silvestri, V. V. T. Padil, M. Řezanka, M. Černík and M. Jaroniec, *Adv. Colloid Interface Sci.*, 2022, **310**, 102807.